Magnetotransport studies of the single and bilayer two dimensional electron gas in the quantum Hall regime

Galistu, G.M.

Publication date
2010

5. Irrelevant critical behavior

5.1 Introduction

Having discussed the relevant critical behavior in *Chap.* 4, we here focus on the irrelevant critical behavior and its irrelevant critical exponent. The meaning of the irrelevant critical behavior within the context of the scaling theory for the QHE is elaborated in *Chap*. 2. The experimental manifestation of this phenomenon will be discussed in this chapter. The deviations from quantization that we would like to determine in order to probe irrelevant critical behavior are of the order of a few percent of the quantized value h/e^2 of the $\nu = 1$ plateau [1,2,3]. For a perfect homogeneous sample these should be easily detectable using the appropriate measuring equipment. A discussion of the method used for these experiments is found in *Chap*. 3 of this thesis. However macroscopic sample inhomogeneities like gradients and especially contact misalignment thwart the proper observation of the deviations from quantization [1]. In this chapter we will discuss the most common ways to deal with these sample imperfections. Next we will show the measured deviations from quantization obtained with the DC method for three electron densities on sample 3388#1-W (n_e = 1.3, 1.8 and 2.0 x10^{15} m^{-2}). Then we report the analysis that has been performed on the data to extract the irrelevant critical behavior and the corresponding critical exponents. The analysis consists mainly of collapsing different data-sets (each data-set belonging to a different filling factor) onto one single curve, of which the general shape follows from the expected power-law behavior. It turns out that after applying a temperature dependent shift in filling factor of the measured curves the data-collapse improves. Finally we present the flow diagram calculated for the PI transition measured on the 2DEG for n_e = 1.8 x 10^{15} m^{-2}. This diagram is compared with experimentally obtained flow lines [5]. The evolution of our understanding of the flow diagram will briefly be elaborated.

5.2 Dealing with sample inhomogeneities and contact misalignment

The core of our task is to probe critical behavior in the quantum Hall regime, or more specifically: irrelevant quantum critical behavior in the Hall resistivity nearby the PI-transition. As a more ambitious task we also want to show that this quantum critical behavior is universally valid, meaning that it is sample independent and is obeyed by all 2DEGs, as long as the sample related criteria for scaling are satisfied. In order to proof universality there are different routes: One may take several suitable samples, possibly made out of different semiconductor materials, and carry out measurements on all of them. One may also take a sample in which the carrier density is tunable. In this case reaching a higher density by illuminating the 2DEG with infra-red light at low temperatures creates a situation which is equivalent to a different sample. The lack of availability of samples and that fact that not all available samples are suitable has limited us to the second option. Therefore, all the measurements described in this chapter were performed on an InGaAs/GaAs Quantum Well with tunable carrier density. An image of this sample is shown in *Fig*. 3.11 of chapter three. Unfortunately most samples are non-ideal 2-DEGs because of macroscopic sample inhomogeneities. This means that the electron density throughout the 2DEG is not constant, but varies with place. If we consider the expression for the B_c-values where the transitions occur, were ν is the filling factor, e is the electron charge and n_e is the electron density,

$$B_c = \frac{h \cdot n_e}{e \cdot \nu} \tag{5.1}$$

it is clear that an electron density that is not constant throughout the 2DEG will have drastic consequences. As result of this the same transition will occur for different values of the magnetic field in different parts of the 2DEG. So instead of one filling factor for the whole 2DEG, we have to deal with a local filling factor: $\nu(\mathrm{r}) = \nu_0 + \nu_x \times x + \nu_y \times y$. This results from an asymmetric growing technique of the semiconductor structure and an inhomogeneous freezing in of the impurities responsible for the disorder potential upon cooling down. An extended study on sample inhomogeneities can be found in *Refs*. [1,4]. Another sample imperfection we have to deal with is the so called contact misalignment. Due to microscopic differences in the electron-density nearby two geometrically perfectly opposing contacts, these contacts effectively are slightly misaligned. The main consequence of this is an admixture of resistivity components. It has been shown that there

are several ways to take care of sample inhomogeneities and contact misalignment [1-4]. These different ways and why a specific way has our preference in the case described here will be briefly discussed next. The first way to deal with these sample imperfections is the stretch-tensor formalism developed by Pruisken [3,4]. According to this an ideal Hall bar geometry can be represented as a rectangular shape with sides $L \times W$ and a homogeneous distribution of carrier density 'n_e'. A non-ideal Hall bar, that is a Hall bar with contact misalignment and macroscopic inhomogeneities can be mapped onto the same rectangular shape where the y-axis is tilted by an angle θ and where the electron density is spatially dependent: $n_e\ (x, y)$, i.e stretched out. See *Fig*. 5.1.

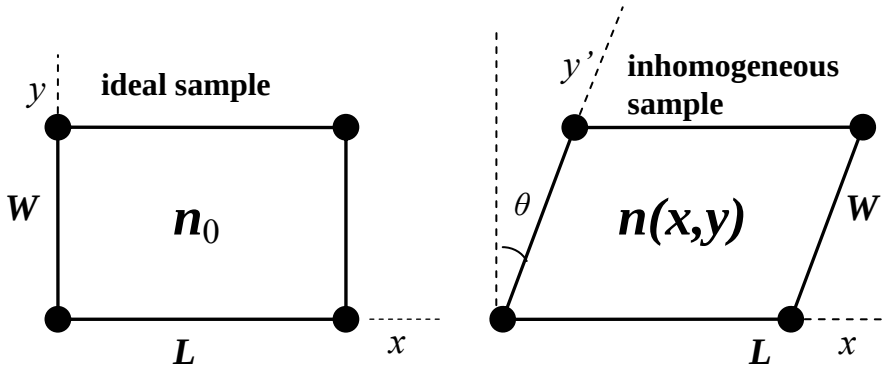

Figure 5.1 Schematic representation of the stretch tensor 'S_{ij}' Left an ideal sample with sides $L \times W$ and a homogeneous distribution of carrier density n_e. Right an inhomogeneous sample with a spatially dependent electron density n_e (x,y) and contact misalignment that can be represented by the angle θ.

It has been shown that any pair of components ρ_{xx}, ρ_{xy} measured on a non ideal sample, can be expressed in the following way [4]:

$$\rho_{ij} = S_{ij}\rho_0 + \varepsilon_{ij}\rho_H^{(0)} + S_{ij}'\rho_H^{(1)} \tag{5.2}$$

where ρ_H and ρ_0 are the intrinsic transport coefficients. $\rho_H^{(0)}$ and $\rho_H^{(1)}$ are both odd under a change of the polarity in B:

$$\rho_H^{(0)}(B) = -\rho_H^{(0)}(-B)$$
$$\rho_H^{(1)}(B) = -\rho_H^{(1)}(-B) \tag{5.3}$$

The intrinsic transport coefficients as a function of $X = (T/T_0)^{-\kappa}$ are:

$$\rho_0(X) = e^{-X+O(X^3)}$$

$$\rho_H(X,\eta) = \rho_H^{(0)} + \rho_H^{(1)}(X,\eta) \tag{5.4}$$

with $$\rho_H^{(0)} = 1, \qquad \rho_H^{(1)}(X,\eta) = \eta(T)\rho_0(X) \tag{5.5}$$

The effects of sample inhomogeneities (density gradients and contact misalignment) are all contained in:

$$S_{ij} = \frac{1}{\cos\theta}\begin{bmatrix} \rho_c & \sin\theta \cdot e^{\frac{\delta\nu_x}{\nu_0(T)}} \\ -\sin\theta \cdot e^{-\frac{\delta\nu_y}{\nu_0(T)}} & \rho_c^{-1} \end{bmatrix} \tag{5.6}$$

$$S_{ij}' = \frac{1}{\cos\theta}\begin{bmatrix} 0 & \sin\theta \cdot e^{\frac{\delta\nu_x}{\nu_0(T)}} \\ -\sin\theta \cdot e^{-\frac{\delta\nu_y}{\nu_0(T)}} & 0 \end{bmatrix} \tag{5.7}$$

Now consider that the ρ_{xy} data for constant T can be split in a symmetric and an antisymmetric part

$$\rho_{xy}(B) = \rho_H(B) + \rho_{xy}^s \tag{5.8}$$

in which ρ_{xy}^s is only an admixture of the R_{xx} component. The ρ_{xy}^s data is taken from a different part of the sample than the R_{xx} data, which is like a global average of the sample resistance. In case of macroscopic sample inhomogeneities there will be a noticeable difference between the critical fixed point ν_c obtained from the R_{xx} data, and $\tilde{\nu}_c$ obtained from the ρ_{xy}^s data (from now on all the parameters obtained from the ρ_{xy}^s data will be shown with a tilde). If we assume a spatially dependent filling factor $\nu(r) = \nu_0 + \nu_x x + \nu_y y$, than the stretch tensor S_{ij} is given by

$$S_{ij} = \frac{1}{\cos\theta}\begin{bmatrix} 1 & \sin\theta \cdot e^{\frac{\varepsilon_x \nu}{\nu_0(T)}} \\ -\sin\theta \cdot e^{-\frac{\varepsilon_y \nu}{\nu_0(T)}} & 1 \end{bmatrix} \tag{5.9}$$

where $\varepsilon_x = \pm\nu_x \frac{L}{2\nu}$ and $\varepsilon_y = \pm\nu_y \frac{W}{2\nu}$. These are taken as fixed quantities representing the relative uncertainties in the electron density in the *x* and *y* directions. From *Eqs.* (5.6), (5.7) and (5.8) it follows that

$$\rho_{xy}^{S}(B,T) = \tan\theta \cdot e^{\frac{\varepsilon_x \nu}{\nu_0(T)}} \rho_0(X) = \tan\theta \cdot \rho_0(\widetilde{X}) \tag{5.10}$$

where $\widetilde{X}$ is the local scaling variable

$$\widetilde{X} = \frac{\nu - \widetilde{\nu}_c}{\widetilde{\nu}_0(T)} \tag{5.11}$$

and

$$\widetilde{\nu}_c = \frac{\nu_c}{1+\varepsilon_x} \tag{5.12}$$

$$\widetilde{T}_0 = T_0(1+\varepsilon_x)^{1/\kappa} \tag{5.13}$$

are the local equivalents of ν_c and T_0 when there is only a measurable gradient in the *x*-direction. ε_x can be determined from the experimental data by using the distance between the local fixed point '$\widetilde{\nu}_c$' and the global fixed point 'ν_c'. A value for tan θ can be obtained by plotting $\frac{\rho_{xy}^{S}}{\rho_0(X)}$ and than fitting with tanθ exp*(X)*. In the abovementioned we have tried to explain how to use the abstract concept of the stretch tensor in order to obtain an idea about the contact misalignment and the density gradient in the Hall bar. Another way to deal with the inhomogeneities is just to extract all the parameters needed for the data analysis from the 'local' situation. Instead of using the ρ_0 data for extracting values like ν_c, κ and T_0 we use the ρ_{xy}^{s} data. We have applied both methods. In the final analysis however we have chosen for the second method. Reason for this is that in this way we can directly extract the 'local behavior' of the 2DEG for the small region of interest to us. We can do this without the concern of how the inhomogeneity profile of the 2DEG really looks like, whether it is a gradient in the *x*-direction, in the *y*-direction, in both directions or maybe something far more complicated. This in contrast to the first method in which we are bound to the assumption that we are dealing with a linear variation in the electron density, and based on this assumption we try to 'reconstruct' the local situation in the region of interest.

5.3 DC results for three electron densities of the 2DEG

In the course of our experiments the magnetotransport data for three electron densities have been examined: 1.3, 1.8 and 2.0 × 10^{15} m^{-2}. First we will elaborate the procedure of data analysis used for the lowest density. Then we will show the results obtained for all three densities. In all the DC measurements described in this chapter the set values for the Delay time and the NPLC's where 350 ms and 15, respectively. The Moving Filter was set to 4 (see *Chap*. 3). This corresponds to a time constant of around 4 seconds and a 'frequency' of around 0.8 Hz. In *Fig*. 5.2 we show the longitudinal resistance near the PI transition in a semi-logarithmic plot:

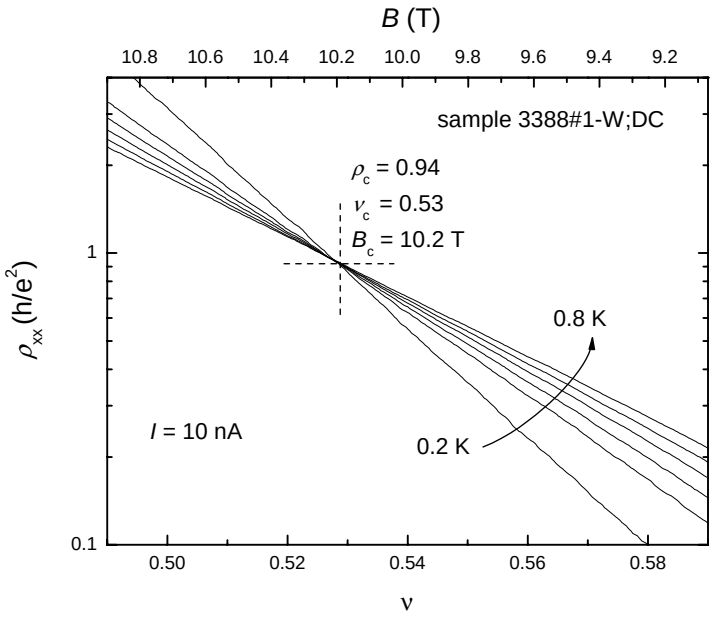

Figure 5.2 PI-transition of sample 3388#1-W for the longitudinal resistivity at six temperatures (T = 0.2, 0.4, 0.5, 0.6, 0.7 and 0.8 K) in a semi-logarithmic plot as a function of filling factor (lower axis) and magnetic field (upper axis); n_e = 1.3x10^{15} m^{-2}. The measurement current was 10 nA.

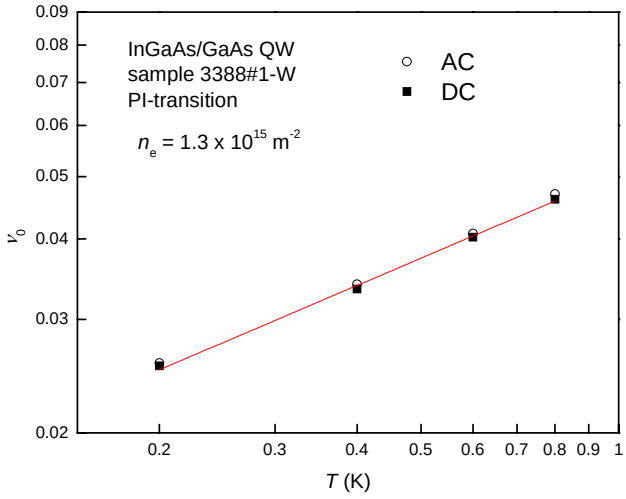

Figure 5.3 Temperature dependence of the parameter ν_0 in a double logarithmic plot of sample 3388#1-W. Both the AC and DC cases are shown.

In *Fig*. 5.3 we show ν_0 as a function of T for both the AC and DC measurements. For this density, fitting the data points with a linear fit gives a similar slope for both the AC and DC method: 0.43. Note that the critical filling factor for the PI transition $\nu_c = 0.53$. This value is higher than the theoretically expected value of $\nu_c = 0.5$. The reason for this is the non-zero overlap between the Landau levels [1]. *Figs*. 5.2 and 5.3 reflect the 'global' behavior of the 2DEG. In fact it should be seen as the average behavior over the whole area of the 2DEG between the resistivity contacts.

Due to inhomogeneities local behavior in a specific region of the 2DEG does not need to be the same as the global behavior. Since we are interested in the critical behavior of the Hall resistivity, our region of interest is the one between two opposite Hall contacts. One way to obtain experimental insight in this local region is provided by one of the sample imperfections: the contact misalignment. Since $\rho_{xy,s}$ is in fact the admixture of the longitudinal resistance component in the Hall component (*Eq*. 5.8), it is possible to do the same analysis on $\rho_{xy,s}$ as we did on ρ_{xx}. *Fig*. 5.4 shows the crossing point of the $\rho_{xy,s}$ data in a semi-log plot for seven temperatures. Note that the critical filling factor is significantly higher than for the ρ_{xx} data: $\nu_c = 0.6$. Also B_c is lower than for the ρ_{xx}- case: $B = 9.8$ T. This

indicates that the electron density between the Hall- contacts is lower than the averaged density over the whole 2DEG. From the $\rho_{xy,s}$ -curves shown in *Fig*. 5.4 we again extract ν_0 and trace ν_0 vs. T in *Fig*. 5.5.

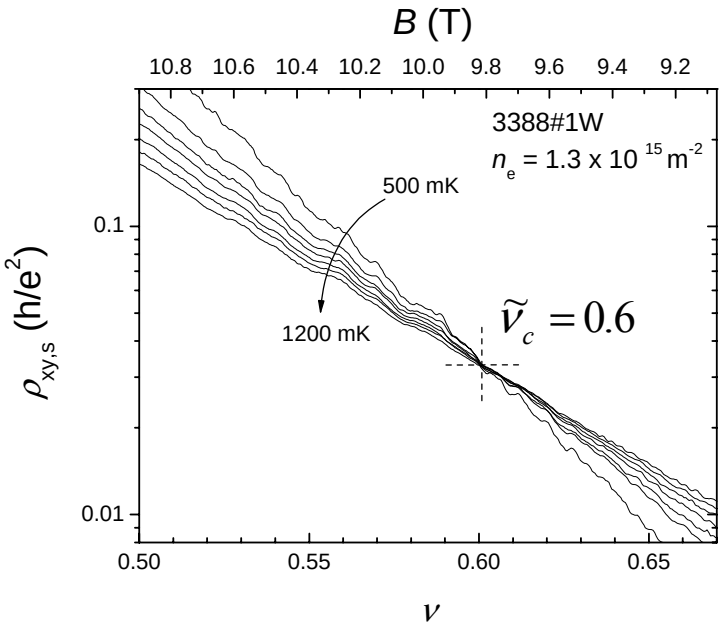

Figure 5.4 PI transition for the longitudinal resistivity component measured at the Hall contacts ($\rho_{xy,s}$) for seven temperatures in a semi-logarithmic plot (T = 0.5, 0.7, 0.8, 0.9, 1.0, 1.1 and 1.2 K) as a function of filling factor (lower axis) and magnetic field (upper axis). The field polarity is positive.

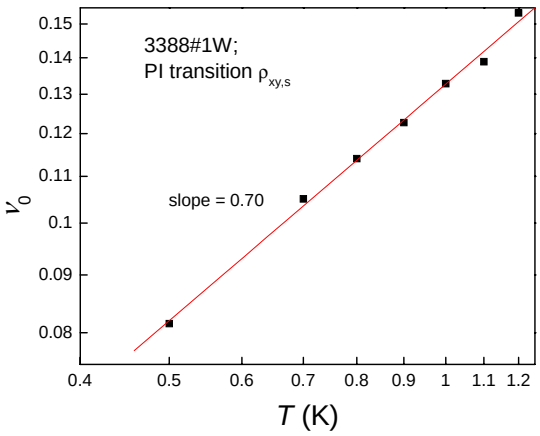

Figure 5.5 ν_0 vs. T for the PI transition of $\rho_{xy,}$

Fig. 5.5 shows that the slope of the temperature dependence of ν_0 for $\rho_{xy,s}$ differs a lot from the one found for the ρ_{xx}-data (*Fig.* 4.8). This illustrates clearly how the local inhomogeneity situation between the Hall contacts can distort critical behavior. The parameter of most interest to us in our further discussion is $\tilde{\nu}_c$, since this is the filling factor at which the PI transition occurs for ρ_H. We recall the scaling functions [2] for the critical behavior of ρ_H at the PI transition:

$$\rho_H = 1 + \eta(T)\rho_0(\tilde{X}), \tag{5.14}$$

with $$\eta(T) = \left(\frac{T}{T_1}\right)^{y_\sigma}; \quad \rho_0(\tilde{X}) = e^{-\tilde{X} - O(\tilde{X}^3)}; \tag{5.15}$$

where $$\tilde{X} = \frac{(\nu - \tilde{\nu}_c)}{\nu_0(T)} \tag{5.16a}$$

and $$\nu_0(T) = \left(\frac{T}{\tilde{T}_0}\right)^{\kappa} \tag{5.16b}$$

In *Fig*. 5.6a we show ρ_H after symmetrizing for both field polarities. Using $\nu = \frac{h \cdot n_e}{e \cdot B}$ and substracting $\tilde{\nu}_c$ we can plot ρ_H versus $\Delta\nu$ (*Fig.* 5.6b). Notice the noisy behavior of the T = 0.5 K curve. This is because the deviation from quantization is the smallest for this temperature, while the diverging of the $\rho_{xy,s}$ for both field polarities is the largest here. This gives a very bad signal to noise ratio.

Eq. 5.15 tells us that the deviation from quantization displays power law behavior. For $\Delta\nu$ = 0 this power law behavior is completely described by the η (T) term. For $\Delta\nu \neq 0$ this power law behavior is the product of η (T) and $\rho_0(\tilde{X})$. The data shown in *Fig*. 5.6b can be plotted in a different way: taking a fixed value for $\Delta\nu$ and plotting the temperature dependence of ρ_H-1 for this value. This is shown in *Fig.* 5.7 for seven values of $\Delta\nu$.

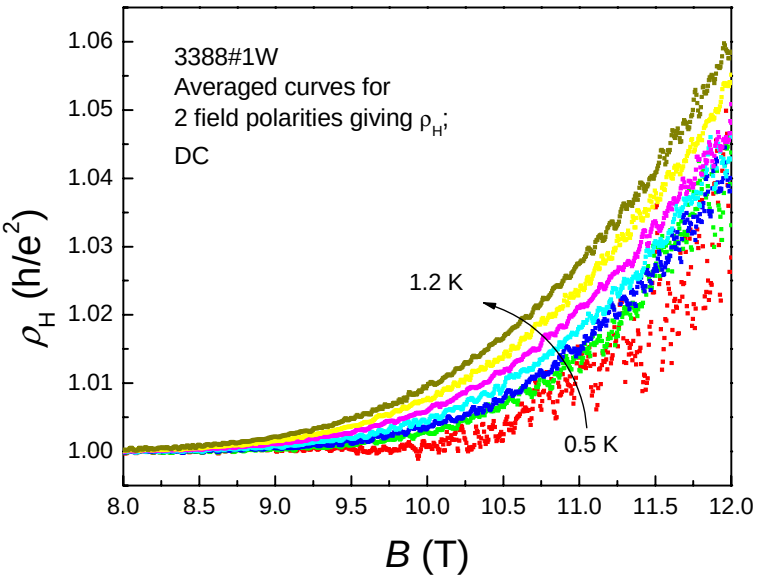

Figure 5.6a Critical behavior of ρ_H at the PI-transition for T = 0.5, 0.7, 0.8, 0.9, 1.0, 1.1 and 1.2 K.

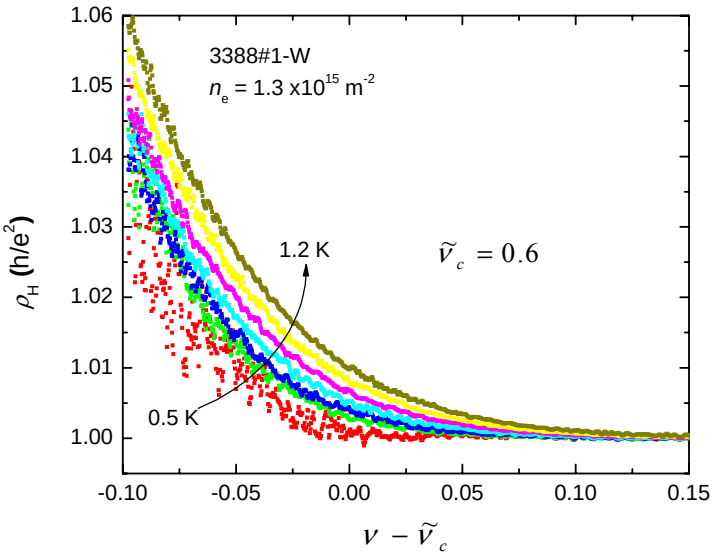

Figure 5.6b ρ_H vs. at T = 0.5, 0.7, 0.8, 0.9, 1.0, 1.1 and 1.2 K.

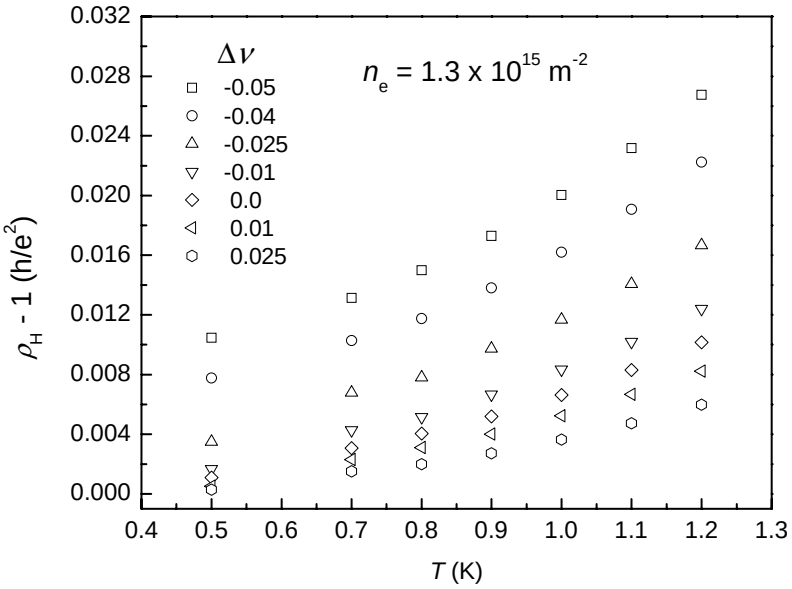

Figure 5.7 ρ_H -1 vs. *T* for seven values of $\Delta\nu$.

From *Eq*. 5.14 it follows that dividing out $\rho_0(\tilde{X})$ from the curves for constant $\Delta\nu$ in *Fig*. 5.7 will give a collapse of the data on $\eta(T)$. The parameters $\tilde{\nu}_c$, and $\tilde{T}_0$ present in $\rho_0(\tilde{X})$ are obtained in the following way: $\tilde{\nu}_c$ follows from the crossing point of the $\rho_{xy,s}$ curves as mentioned above. For $\tilde{T}_0$ and κ the following has been done. The data points in *Fig*. 5.7 can be seen as seven one dimensional (1D) functions $\rho_H(T)$ - 1 for different constant values of $\Delta\nu$. What we can do is map these seven 1D datasets on a 2D data- surface so that a 2D function $\rho_H(T,\Delta\nu)$-1 describes all the data-points. The function used is

$$\rho_H - 1 = \left(\frac{T}{T_1}\right)^{y_\sigma} e^{\frac{-(\Delta\nu-\delta\nu_c)}{(T/T_0)^\kappa}}, \qquad (5.17)$$

where $\delta\nu_c$ is the deviation from $\tilde{\nu}_c$, that can be temperature dependent. The fit is shown in *Fig*. 5.8.

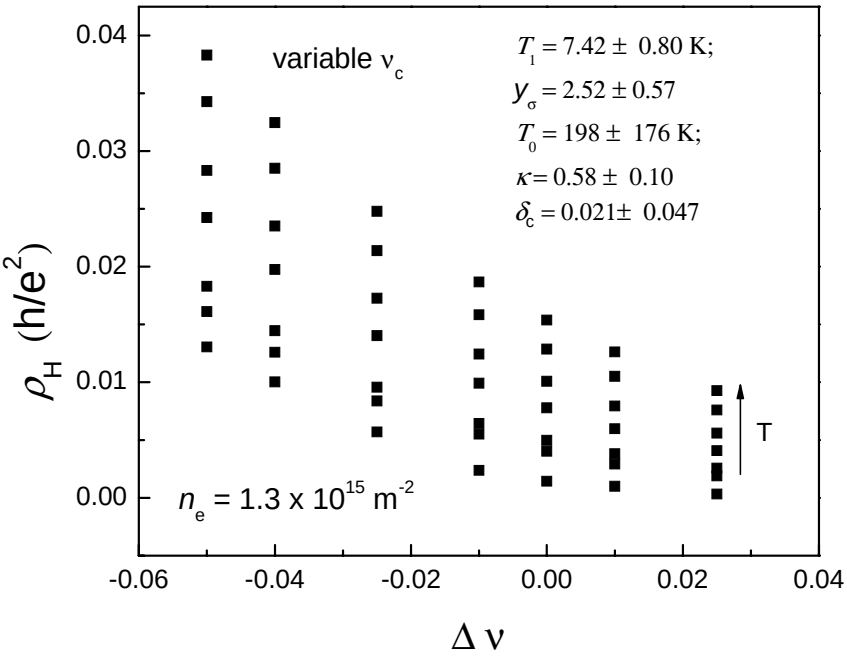

Figure 5.8 two dimensional display of all the data points shown in *Fig*. 5.7 using *Eq*. 5.17.

Important in this method is that we just get one set of the 5 fit parameters. These parameters can be considered an optimum based on all the information contained in the seven 1D datasets mentioned before. Using the values for $\widetilde{T}_0$ and κ we can apply the data collapse on the data sets in *Fig*. 5.7.

The values for T_1 and y_σ found after fitting with $\eta(T)$ are 11.8 K and 1.8 resp. These values are different than the ones mentioned in *Ref*. [1] for the same wafer: 4.5 K for T_1 and 2.6 for y_σ.

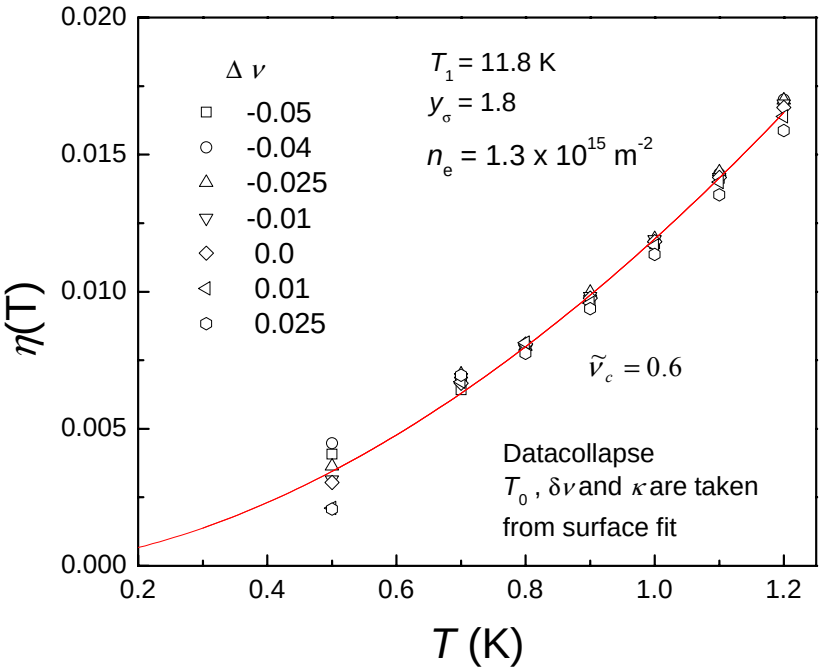

Figure 5.9 Collapse of the ρ_H data (see *Fig.* 5.7) onto a single curve $\eta = (\rho_H - 1)/\rho_o$ ($\widetilde{X}$) vs. T for different values of $\Delta\nu$. T_0, κ and $\delta\nu$ are taken from a 2D fit like in *Fig.* 5.8.

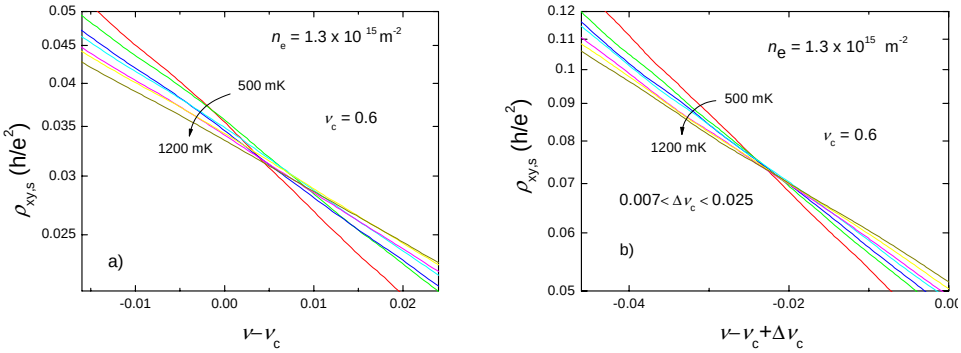

Figure 5.10a) The uncorrected situation for the $\rho_{xy,s}$ data. We can see a poorly defined crossing point and the data show a lack of symmetry around this 'crossing point'. *b*) The corrected situation. The data is smoothed using the 'adjacent averaging' procedure in Origin.

The $\rho_{xy,s}$ data do not show a well defined crossing point as shown in *Fig.* 5.10a. However, this can be obtained by a small temperature dependent shift $0.007 \leq \Delta\nu_c \leq 0.025$ as shown in *Fig.* 5.11b. The shift is the smallest for the highest temperature.

Also the data around the crossing point are now much more symmetric as is required by the condition of particle-hole symmetry [2]

$$\rho_0(X) = \rho_0^{-1}(-X) \tag{5.18}$$

Repeating the procedure described above using the shifted curves of ρ_H gives the data collapse shown in *Fig.* 5.11.

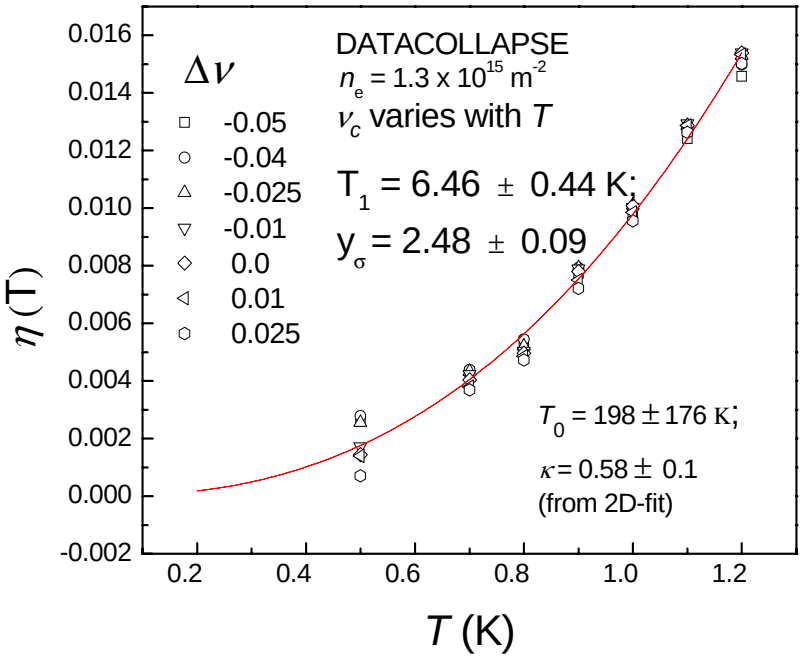

Figure 5.11 Collapse of the ρ_H data (see *Fig.* 5.7) onto a single curve $\eta = (\rho_H - 1)/\rho_o$ ($\tilde{X}$) vs. T for different values of $\Delta\nu$. T_0, κ and $\delta\nu$ are taken from a 2D fit like in *Fig.* 5.8. The original curves of ρ_H have been given a temperature dependent shift. $n_e = 1.3 \times 10^{15}$ m^{-2}.

For the other two densities the results are shown on the next pages. We will limit ourselves here to show the final results only.

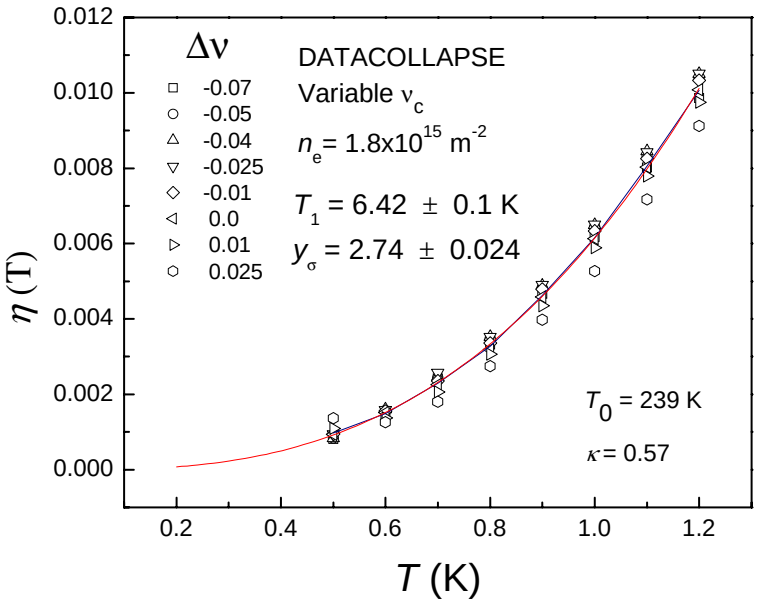

Figure 5.12 Collapse of the corrected ρ_H data onto a single curve $\eta = (\rho_H - 1)/\rho_o$ ($\widetilde{X}$) vs. T for different values of $\Delta\nu$. T_0, κ and $\delta\nu$ are taken from the 2D fit. $n_e = 1.8 \times 10^{15}$ m^{-2}.

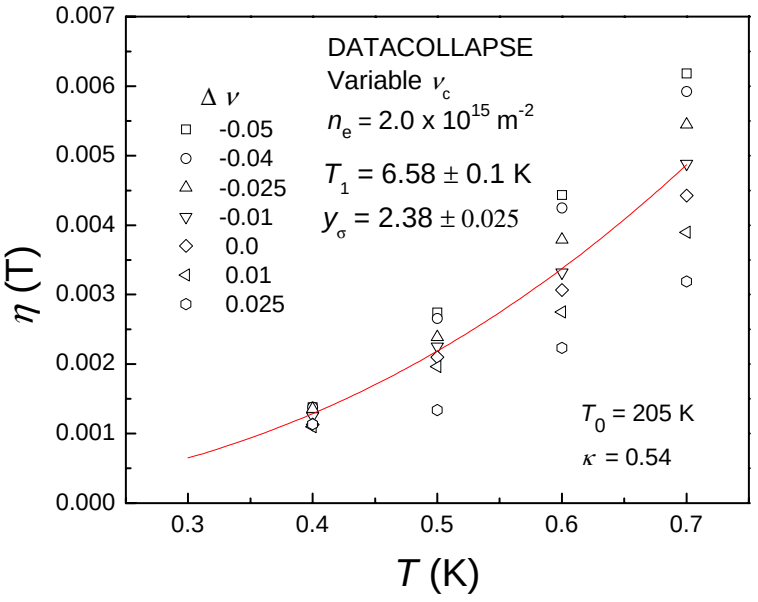

Figure 5.13 Collapse of the corrected ρ_H data (see *Fig.* 4.12) onto a single curve $\eta = (\rho_H - 1)/\rho_o$ ($\widetilde{X}$) vs. T for different values of $\Delta\nu$. T_0, κ and $\delta\nu$ are taken from the 2D fit. $n_e = 2.0 \times 10^{15}$ m^{-2}.

Notice that the datacollapse for $n_e = 2.0 \times 10^{15}$ m^{-2} shows more spread than for the previous densities. This is because we only could measure until 0.7 K for this density. In this low temperature range the effect is smaller and consequently the relative error is bigger.

5.4 Flow diagrams

By plotting σ_{xx} *versus* σ_{xy} for the *PI* transition using the tensor relation

$$\sigma_{xx} = \frac{\rho_{xx}}{\rho_{xx}^2 + \rho_{xy}^2}, \quad \sigma_{xy} = \frac{\rho_{xy}}{\rho_{xx}^2 + \rho_{xy}^2} \tag{5.19}$$

we construct the renormalization group flow diagram. Unfortunately, we were not able to directly measure the flow lines for $T > 1.2$ K. However, by making use of the universal scaling functions (see chapter 2)

$$\sigma_0(X,\eta) = \frac{e^{-X}}{1 + 2\eta e^{-X} + e^{-2X}} \tag{5.20}$$

$$\sigma_H(X,\eta) = \frac{1 + \eta e^{-X}}{1 + 2\eta e^{-X} + e^{-2X}} \tag{5.21}$$

with parameters κ, T_0, y_σ and T_1 as obtained from the experiment, we can plot the flow diagram up to higher temperatures. This most important diagram is shown in *Fig*. 5.14. The flow lines emerge from the Self Consistent Born Approximation (SCBA) curve [5] near $T \approx T_1 = 6.5$ K [2,3]. The scaling regime is entered below 4.2 K and is depicted by the (symmetric) upward flow towards the asymptotic semicircle ($T \rightarrow 0$) $\sigma_0^2 + (\sigma_H - e^2/2h)^2 = (e^2/2h)^2$ for the plateau-to-insulator transition.

The way we understand the complete flow diagram (i.e. displaying both relevant and irrelevant critical behavior) and how it should be interpreted has changed drastically since the first experimental study of scaling [5]. An early calculation of the flow diagram obtained from the dilute instanton gas method can be found in *Ref*. [6]. The only aspect that has remained unaltered in time is the presence of the semicircle for $T = 0$. This has been measured on all types of samples [7], regardless of their quality or even whether they displayed scaling properties or not. The only two criteria that need to be met in order to obtain a semicircle for the *PI* transition are a Hall resistance that remains quantized and an

exponentially diverging longitudinal resistance. In *Fig*. 5.14b) we reproduce an early flow diagram obtained for the 2→1 plateau-plateau transition [5]. When compared to our calculated flow diagram, based on the experimentally obtained parameters for the *PI* transition (sample 3388#1-W at $n_e = 1.8 \times 10^{15}$ m^{-2}), the differences are striking. In the early results, the trajectory of the flow lines towards the semicircle has been given a wrong interpretation. Also the expected particle-hole symmetry, causing the critical point to occur at half integer values of σ_{xy} was missing.

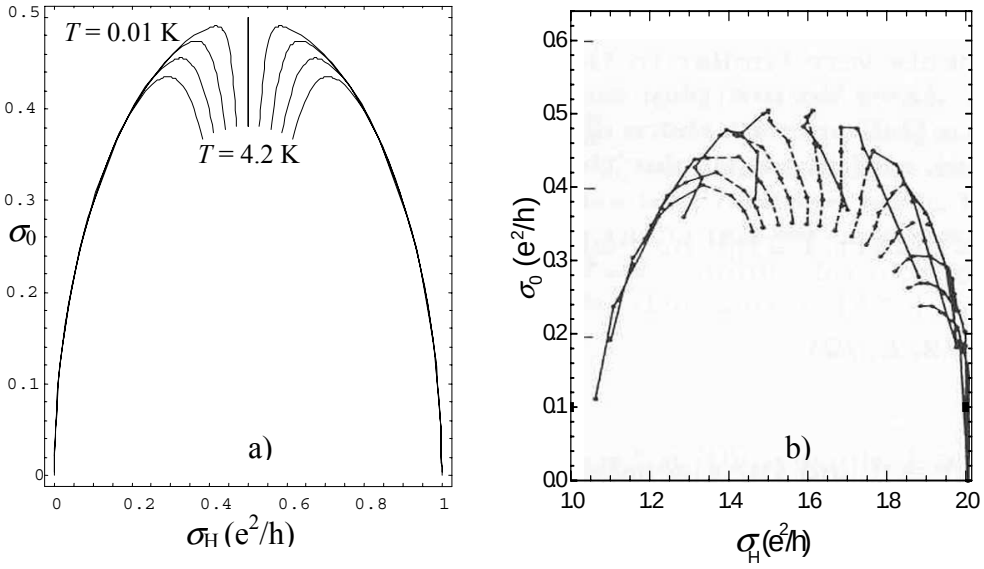

Figure 5.14 a) Temperature-driven flow lines with 0.01 < T < 4.2 K near the *PI* transition. The experimental values $T_0 = 202$ K, $T_1 = 6.4$ K, $\kappa = 0.53$ and $y_\sigma = 2.74$ have been used. b) Experimental σ_{xx} and σ_{xy} plotted as T-driven flow lines from T = 10 to 0.5 K for the *PP* transition 2→1 as taken from *Ref*. [5]. The dashed lines are from 10 to 4.2 K and the solid lines from 4.2 to 0.5 K.

The differences in the flow diagrams illustrate very well how our understanding of the process of scaling has evolved during the last decades. Initially the flow in the temperature range 4.2-10 K towards the semicircle in *Fig*. 5.12b) was attributed to the broadening of the Fermi-Dirac distribution with increasing temperature. Also it was thought that in the low-temperature regime 0.5-4.2K, where thermal broadening is much smaller than the Landau level broadening, proper scaling was represented in the flow diagram by the downward flow accompanied by a - not understood - decrease of σ_0 with temperature. Later, after having found experimental evidence for the already theoretically predicted irrelevant critical behavior, it turned out that the upward flowing of the conductivity lines towards the semicircle does represent genuine scaling behavior. The assumption that this had to be attributed to Fermi-Dirac broadening is wrong: Fermi-Dirac broadening does not play a significant role in the scaling regime. The major breakthrough in connecting the measured diagrams to the theoretically predicted ones, came through the understanding of how macroscopic inhomogeneities influence the observation of critical behavior [2,3,4]. It was shown [2,3,4] that *PP* transitions in general are much more sensitive to macroscopic sample inhomogeneities than PI transitions and as a result do not give proper flow diagrams. Thus only by measuring the *PI* transition, and considering both relevant and irrelevant critical behavior and the effect of sample inhomogeneities, the final flow diagram as shown in *Fig.* 5.14a can be obtained.

5.5 Conclusions

- The irrelevant critical behavior in the Hall resistance ρ_H near the PI transition was measured on an InGaAs/GaAs quantum well for three different electron densities. The data are analyzed within the scaling theory using a newly developed data collapse procedure. The extracted values for the irrelevant critical exponent y_σ and the temperature T_1 below which scaling sets in attain similar values for the three electron densities as shown in *Table* 5.1. The value $y_\sigma \approx 2.5$ corresponds well with the values reported in the literature [1,3].

Table 5.1 Value of T_1 and y_σ for $n_e = 1.3$, 1.8 and 2.0×10^{15} m^{-2}.

n_e	T_1 (K)	y_σ
1.3 x 10^{15} m^{-2}	6.46	2.48
1.8 x 10^{15} m^{-2}	6.42	2.74
2.0 x 10^{15} m^{-2}	6.58	2.38

- In order to obtain a good data collapse it appeared necessary to apply a small temperature dependent shift of the data in ν. Applying this shift improves the crossing point of the $\rho_{xy.s}$ data (*Fig.* 5.10). The fact that the critical filling factor has a small temperature variation underlines the high degree of macroscopic inhomogeneities in the sample: the filling factor differs when measured in different parts of the sample (compare *Figs* 5.2 and 5.4). The stretch tensor formalism, that assumes a linear variation of the electron density along the Hall bar, could not be used to analyze the data. Instead, we have chosen to look directly at the region of interest in the Hall bar by making use of the $\rho_{xy,s}$ data.

- The flow diagram of the PI transition has been calculated from the scaling functions using the experimental parameters for κ, y_σ, T_0 and T_1 extracted from the data collapse. The flow diagram shows all the properties predicted for genuine scaling: relevant and irrelevant flow, the location of the critical point $(\sigma_H, \sigma_0) = (½e^2/h, ½e^2/h)$ and particle-hole symmetry. The determination of the flow diagram was made possible after unraveling and fully understanding the effect of macroscopic sample inhomogeneities.

5.6 References

[1] L.A. Ponomarenko, *Ph.D Thesis* (University of Amsterdam, 2005), unpublished.

[2] A.M.M. Pruisken, D.T.N. de Lang, L.A. Ponomarenko and A. de Visser, *Solid State Communications* **137** (2006) 540.

[3] D.T.N. de Lang, *Ph. D Thesis* (University of Amsterdam, 2005), unpublished.

[4] B. Karmakar, M.R. Gokhale, A.P. Shah, B.M. Arora, D.T.N. de Lang, A. de Visser, L.A. Ponomarenko and A.M.M. Pruisken, *Physica E* **24** (2004) 187.

[5] H.P.Wei, D.C. Tsui and A.M.M. Pruisken, *Phys. Rev. B* **33** (1985) 1488.

[6] A.M.M. Pruisken, *Phys. Rev. Lett.* **32** (1985) 2636.

[7] M. Hilke, D. Shahar, S.H. Song, D.C. Tsui, Y.H. Xie and M. Shayegan, *Europhys. Letters* **46** (1999) 775.